Low ICI Symbol Boundary Alignment for 5G Numerology Design

MAHYAR NEMATI[1], (Member, IEEE), AND HÜSEYIN ARSLAN[1,2], (Fellow, IEEE)
[1]School of Engineering and Natural Sciences, Istanbul Medipol University, Istanbul 34810, Turkey
[2]Department of Electrical Engineering, University of South Florida, Tampa, FL 33620, USA

Corresponding author: Mahyar Nemati (mnemati@st.medipol.edu.tr)

ABSTRACT Symbol boundary alignment, with respect to waveform selection, has an important impact on the numerology design for fifth-generation mobile applications. The current symbol boundary alignment, along with orthogonal frequency division multiplexing (OFDM) waveform, strongly suffers from intercarrier interference (ICI) especially in unmanned aerial vehicles (UAV) communications. This happens when the mobility causes Doppler effect which results in loss of orthogonality in OFDM. The available solutions for overcoming the ICI problem suffer from high complexity, low spectral efficiency, and incompatibility with the current radio access technologies. This paper presents a novel symbol boundary alignment, called Low ICI Symbol (LICIS) boundary alignment numerology, to avoid the disadvantages of the available solutions. LICIS utilizes large subcarrier-spacing to reduce the ICI power (e.g., around 5-dB ICI power reduction with subcarrier spacing of 30 kHz in high-speed UAV communications). Moreover, LICIS is based on the same reference clock as local thermal equilibrium (LTE) which guarantees its compatibility with the current LTE numerology. In addition, this approach places only one guard-interval at the end of a sequence of OFDM symbols and creates a subslot. This leads to less overhead and preserves the spectral efficiency. Furthermore, a pre-fast Fourier transform (FFT) multipath channel equalizer is considered for removing the intersymbol interference between the OFDM symbols occurring within the subslot. Only one additional FFT and IFFT operations are required for the equalizer which creates an acceptable complexity increment compared to the complexity of other available solutions. Numerical and analytical evaluations show the superior performance of the proposed technique in terms of reliability and spectral efficiency.

INDEX TERMS Doppler, guard interval (GI), intercarrier interference (ICI), numerology, subcarrier-spacing, symbol boundary alignment, unmanned aerial vehicles (UAV), spectral efficiency.

I. INTRODUCTION

Fifth generation (5G) of mobile communication technology is expected to support a wide variety of service requirements, such as high reliability and spectral efficiency in unmanned aerial vehicles (UAV) communications. However, in UAV, the mobility causes Doppler effect which leads to loss of orthogonality in orthogonal frequency division multiplexing (OFDM) [1]. The loss of orthogonality gets even worse in high speed UAV communications, where the speed can go up to hundreds km/h [2]. Consequently, a severe intercarrier interference (ICI) is created which degrades the reliability of the communications severely. Thus, in 5G applications such as high speed UAV, ICI problem needs to be solved.

ICI is the type of frequency distortion due to the interference of other subcarriers with the intended subcarrier [3]. Doppler effect (including Doppler spread and Doppler shift) and carrier frequency offset (CFO) are the main reasons of frequency distortion in frequency dispersive channels. ICI has been always a critical issue in multicarrier-based com-

munications. In the literature, a significant effort has been done in order to overcome it. However, the available solutions have some drawbacks, such as high complexity, low spectral efficiency, and incompatibility with the current radio access technologies.

For instance, in recent surveys and researches, (e.g., [4]–[11] and their references), authors evaluate different types of ICI reduction techniques. However, they suffer from a multi step equalization which results in high complexity. The number of steps is even increased in high speed UAV communications.

Nakamura *et al.* [12] need to estimate the Doppler profile in OFDM reception to cancel the ICI. Besides the complexity of Doppler estimation, fast variation of speed causes to fast variation of Doppler in high speed UAV communications as well. It increases the complexity in high speed applications.

Recently, a technique based on fractional Fourier transform (FrFT)-OFDM was proposed in [13], where authors found the near optimum angle of transform in FrFT-OFDM to
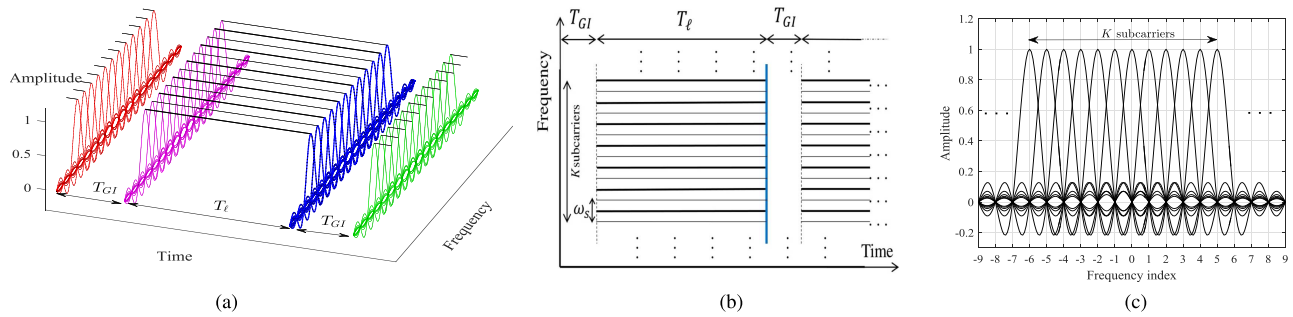
FIGURE 1. Conventional LTE numerology as a reference numerology for LICIS. (a) Time-Frequency domain representation of conventional LTE numerology. (b) Time-Frequency lattice of conventional LTE numerology with reference subcarrier-spacing (Δf_S = 15 kHz). (c) One RB of K orthogonal subcarriers with the reference subcarrier-spacing in absence of Doppler effect.

minimize the bound of ICI power. Besides the complexity issues, angle of transform varies with Doppler severity and the angle approaches zero by increasing Doppler shift which leads to a single carrier transmission.

Another technique, in [14], utilizes small subblock frequency domain equalizations (FDE) by exploiting a pseudo cyclic prefix (CP) technique instead of the real guard interval (GI) in each subblock. However, it requires more FDE steps in high speed communications. Additionally, the reliability of this method is not guaranteed properly due to subtraction of an estimated part from the received signal.

Vakilian *et al.* [15], Jafri *et al.* [16], and Wild *et al.* [17] propose to use filtered subcarrier blocks. They consider each block of subcarriers as a resource block (RB) which can be filtered for transmission. This approach restricts the ICI inside only one RB with the expense of filtering issues. However, ICI problem still exists severely inside that RB.

Utilizing large subcarrier-spacing for high speed users is another solution which is considered in [18]–[20]. However, by increasing the subcarrier-spacing, the symbol duration in the time domain is decreased. Therefore, the number of symbols in one transmission time interval is increased and a greater number of GI is required to prevent intersymbol interference (ISI). Thus, it decreases the spectral efficiency. In addition, using large subcarrier-spacing for high speed users and small subcarrier-spacing for low speed users leads to different symbol durations. It changes the synchronous transmission to an asynchronous transmission [20]. Consequently, handling the asynchronous communications has its own complex solutions (e.g., using filters to suppress the out of band emission of subcarriers to avoid interference between different users).

This paper presents a novel approach, called **Low ICI Symbol boundary alignment numerology (LICIS)**, which reduces the ICI while preserving the spectral efficiency. Contrary to the presented techniques, LICIS does not need a high complex equalization technique or different waveform structure. It only manipulates the conventional symbol boundary alignment numerology to obtain a new symbol boundary alignment which achieves a superior performances. LICIS utilizes large subcarrier-spacing to reduce the ICI power.

In addition, this approach places only one GI at the end of a sequence of OFDM symbols and creates a sub-slot. Therefore, there is no GI between the OFDM symbols inside the sub-slot. It leads to less overhead and consequently preserves the spectral efficiency. Furthermore, a pre-FFT multipath channel equalizer is used to prevent the ISI inside a sub-slot as well. Only one additional FFT and IFFT operations are required for the equalizer which creates an acceptable complexity increment compared to the complexity of other presented solutions. Also, LICIS is based on the same reference clock as LTE which assures its compatibility with the current LTE numerology.

The rest of the paper is organized as follows. In Section II, the system model is explained. Section III evaluates the spectral efficiency of LICIS and the conventional numerologies analytically. In Section IV, the ICI distortion power of LICIS is derived analytically as well. Section V provides the numerical results and comparisons between the LICIS and the conventional symbol boundary alignment numerologies. Finally, Section VI concludes the paper and mentions some of the potentials of the proposed symbol boundary alignment design.

II. SYSTEM MODEL DESCRIPTION AND PROPERTIES

The Symbol boundary alignment has an important impact on the numerology design. The conventional LTE numerology, given in [21], is considered as a reference to propose the LICIS for the 5G numerology. Therefore, in the following, first, an overview of the conventional LTE symbol boundary alignment and its numerology design is given briefly and then the LICIS is explained in integration with that. The complexity of the LICIS is evaluated at end of this section.

A. CONVENTIONAL SYMBOL BOUNDARY ALIGNMENT NUMEROLOGY

Figure 1 shows the conventional LTE numerology, where the data is transmitted on the squeezed orthogonal subcarriers with the same unique subcarrier-spacing and symbol duration (including GI). Let Δf_s and T_ℓ denote the reference subcarrier-spacing and symbol duration without GI, respectively. Note that T_ℓ is an integer number (in discrete domain)
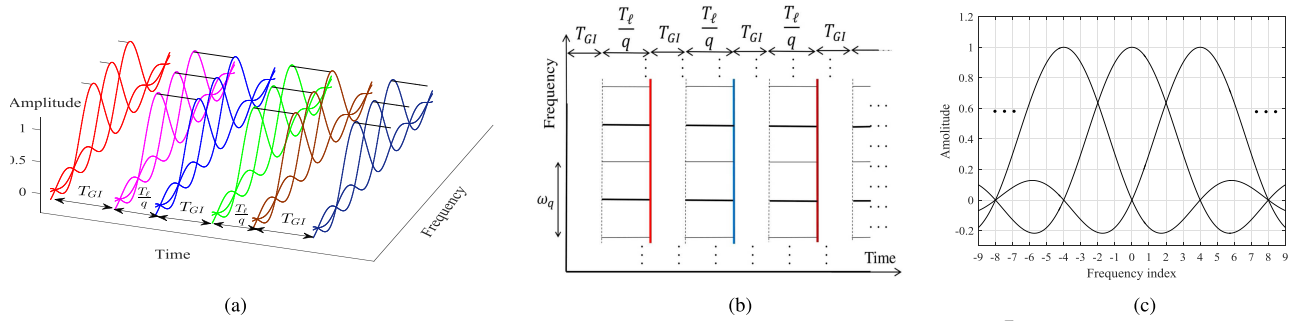
FIGURE 2. Spectral inefficient numerology with large subcarrier-spacing and short symbol duration ($\Delta f_q \sim \omega_q \rightarrow \frac{T_\ell}{q}$). (a) Time-Frequency domain representation of conventional numerology with large subcarrier-spacing. (b) Time-Frequency lattice of conventional numerology with **large subcarrier-spacing** (Δf_q). ($q = 4$). (c) Orthogonal subcarriers with the **large subcarrier-spacing** in absence of Doppler effect ($q = 4$).

FIGURE 3. LICIS structure. **M OFDM symbols with Δf_ρ** are inserted back to back and Only one GI exists at the end of them ($M = \rho = 4$). (a) Time-Frequency domain representation of LICIS. (b) Time-Frequency lattice of LICIS with **large subcarrier-spacing** ($M = \rho = 4$). (c) Orthogonal subcarriers with the **large subcarrier-spacing** in absence of Doppler effect ($\rho = 4$).
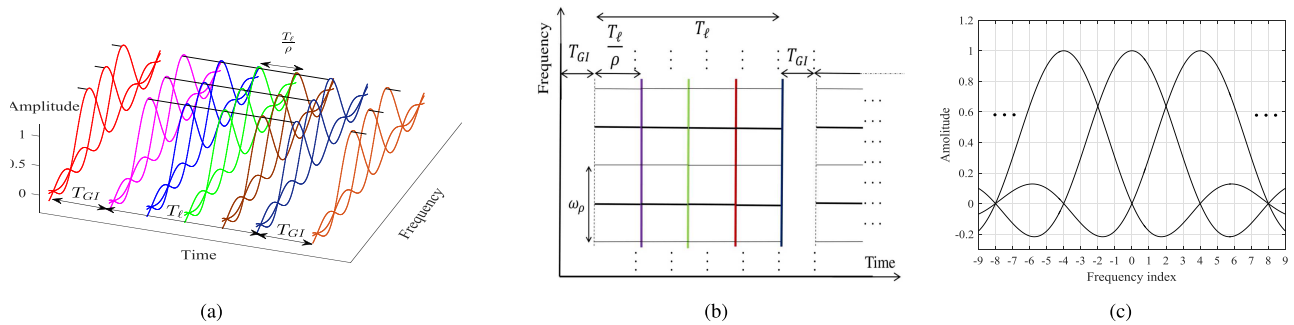
and the real symbol duration is $T_\ell t_s$ where t_s is the sample duration. Moreover, $\Delta f_s = \frac{\omega_s}{2} = \frac{1}{T_\ell}$ where ω_s is the null to null bandwidth (BW) of each Sinc-shaped subcarrier. Each OFDM symbol, constructed by K subcarriers in one RB, is transmitted in one sub-slot with duration of $T_\ell + T_{GI}$ where T_{GI} denote the GI duration. $K(= 12)$ subcarriers, with $\Delta f_s(= 15 \text{ kHz})$, build one RB and every 7 sub-slots, with normal GI length ($\sim 4.7 \, \mu$s), construct one slot ($=0.5$ms) [21]. Also, every two slots construct one transmission time interval (TTI=1 ms).

In the time and frequency dispersive channels, any small shifting of the orthogonal subcarriers, shown in Figure 1(c), destroys the orthogonality of subcarriers and causes distortion as shown in Figure 6 (frequency distortion is explained in section II.B.3). Therefore, the conventional LTE numerology is highly sensitive to the Doppler shift in high speed UAV communications.

In order to overcome the ICI problem, it has been discussed to use different fixed numerologies for different services in a single framework [22]. Particularly, the proposal focuses on using different scaled factor of reference subcarrier-spacing as

$$\Delta f_q = \Delta f_s \times \underbrace{2^m}_{q}, \quad m \in \{\mathbb{N} > 1\},$$

$$\frac{\Delta f_q}{\Delta f_s} = \frac{\omega_q}{\omega_s} = 2^m = q, \tag{1}$$

where the Δf_q and ω_q denote the large subcarrier-spacing of the Sinc-shaped subcarriers and their null to null BW,

respectively. m is an integer number greater than 1 ($\mathbb{N}$ is the set of natural numbers) and q is the ratio of larger subcarrier-spacing over the reference subcarrier-spacing. Equation (1) is the rule of thumb for the scaled subcarrier-spacing (Δf_q) based on the reference subcarrier-spacing (Δf_s). Figure 2 shows such a numerology. In fact, the larger Δf_q results in smaller OFDM symbol duration (T_q) than coherence time (T_c). Therefore, the time-variant channel is changed to the time-invariant channel for the system. However, by increasing the number of symbols in the time domain, a greater number of GI is required and consequently spectral efficiency is decreased.

B. LOW ICI SYMBOL BOUNDARY ALIGNMENT NUMEROLOGY (LICIS)

Figures 3 and 4 show the concept of LICIS where the M OFDM symbols, with large subcarrier-spacing of Δf_ρ, are inserted before one GI in a sub-slot. The sub-slot duration equals $M \frac{T_\ell}{\rho} + T_{GI}$. In LICIS, we have

$$\frac{\Delta f_\rho}{\Delta f_s} = \frac{\omega_\rho}{\omega_s} = \frac{T_\ell}{T_\rho} = \rho, \quad \rho \in \{\mathbb{N} > 1\}, \tag{2}$$

where ω_ρ denotes the null to null BW of Sinc-shaped subcarriers in LICIS. T_ρ is the symbol duration corresponding to the Δf_ρ and ρ is the ratio of large subcarrier-spacing of LICIS over the reference subcarrier-spacing. Utilizing larger subcarrier-spacing decreases the effect of ICI problem in a given BW. Additionally, the smaller number of GI guarantees
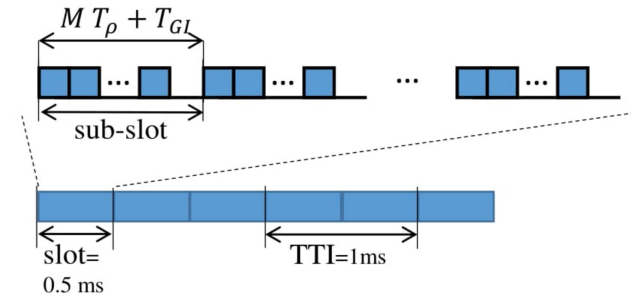
FIGURE 4. Illustration of sub-slot, slot and TTI in LICIS. LICIS is based on the same reference clock as LTE.

the spectral efficiency. Equation (2) assures that LICIS is based on the same reference clock as LTE because the integer and fraction frequency synthesizers offer a simple circuital realization for synthesizing different frequencies based on the same common reference [20], [23]. It results in the compatibility of the LICIS with the current LTE numerology.
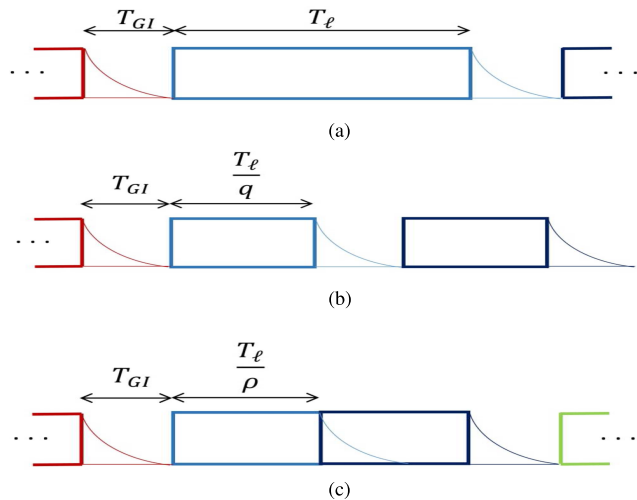

FIGURE 5. The performance illustration of different symbol boundary alignments in a multipath channel. (a) Conventional symbol boundary alignment with Δf_s does not have ISI. (b) Conventional symbol boundary alignment with Δf_q does not have ISI, (q = 2). (c) LICIS has ISI inside one sub-slot ($M = \rho = 2$).

In LICIS, the orthogonality of the subcarriers is saved in the time-invariant channels properly as shown in Figure 3(c). However, the multipath channel causes the ISI between the OFDM symbols in one sub-slot duration as shown in Figure 5. The maximum delay spread of the channel, denoted by $\tau_{\max}$, is assumed to be less than the GI duration. Thus, there is no interference between different sub-slots. In order to remove the ISI inside one sub-slot, a pre-FFT multipath channel equalizer is applied on the whole received sub-slot and therefore, the major effect of time dispersion of wireless multipath fading channel can be removed.

1) GUARD INTERVAL SELECTION
Choosing a suitable GI has an important impact on the numerology design as well. CP and zero-padding (ZP) are the two dominant types of GI in OFDM [24]. Each method has its own advantages and disadvantages. For instance, CP requires

more power consumption than ZP. Also, unlike CP-OFDM, ZP-OFDM guarantees symbol recovery and assures FIR equalization of FIR channels regardless of the channel null locations [25]–[27]. However, ZP-OFDM requires more complex receiver. Muquet *et al.* [25] propose a technique called ZP-FAST equalizer which has an acceptable complexity at the receiver side. In this study, due to utilizing the pre-FFT equalizer which is derived from ZP-FAST equalizer, ZP is considered as the GI (the equalization is explained in section II.B.4). Additionally, by using the ZP, the duration of the loaded signal is MT_ρ which is shorter than $MT_\rho + T_{\mathrm{GI}}$ in the CP-used signal. It results in less ripples in power spectrum density (PSD) of the transmitted signal in ZP-OFDM and achieves better spectral mask efficiency.

2) LICIS CONSTRUCTION
Let $\tilde{\mathbf{d}}_\mu$ denote a stream of independent and identically distributed (i.i.d.) data symbols with zero mean and variance of σ_d^2 for the μth user in the frequency domain. Similar to the conventional LTE numerology, $\tilde{\mathbf{d}}_\mu$ is divided into N_{RB} sub-streams with length of K and denoted by $\tilde{\mathbf{d}}_{\mu,N}$ where $N \in \{1, 2, \cdots, N_{RB}\}$. Therefore, the total number of used subcarriers equals $R = K \times N_{RB}$. Then, we have

$$\tilde{\mathbf{d}}_{\mu,N} \subset \tilde{\mathbf{d}}_\mu = [\tilde{\mathbf{d}}_{\mu,1}^T, \tilde{\mathbf{d}}_{\mu,2}^T, \cdots, \tilde{\mathbf{d}}_{\mu,N_{RB}}^T]^T, \qquad (3)$$

where $(.)^T$ represents transpose operation. The symbols of Nth RB are inserted in the desired subcarriers by matrix $\mathbf{B}_N$. $\mathbf{B}_N \in \{0, 1\}^{\mathfrak{L} \times K}$ is the mapping matrix for N^{th} RB where $\mathfrak{L} = MT_\rho = M\frac{T_\ell}{\rho}$. The transmitted signal for the Nth RB denoted by $\mathbf{X}_{\mu,N}$ is expressed as

$$\mathbf{X}_{\mu,N}^\iota = \mathcal{F} \, \mathbf{B}_N \, \tilde{\mathbf{d}}_{\mu,N}^\iota, \qquad (4)$$

where ι denotes the ιth sub-slot with length of $\mathfrak{L} + T_{GI}$ including M OFDM symbols with subcarrier-spacing of Δf_ρ and one GI. Matrix $\mathcal{F}$ in (4) is expressed as

$$\mathcal{F} = \begin{bmatrix} \mathbf{F}_{T_\rho}^{-1} & \mathbf{O}_{T_\rho} & \cdots & \mathbf{O}_{T_\rho} \\ \mathbf{O}_{T_\rho} & \mathbf{F}_{T_\rho}^{-1} & \cdots & \mathbf{O}_{T_\rho} \\ \vdots & \ddots & \ddots & \vdots \\ \mathbf{O}_{T_\rho} & \cdots & \cdots & \mathbf{F}_{T_\rho}^{-1} \\ \mathbf{O}_{T_{GI}} & \cdots & \cdots & \mathbf{O}_{T_{GI}} \end{bmatrix}_{(\mathfrak{L}+T_{GI}) \times \mathfrak{L}}, \qquad (5)$$

where $\mathbf{F}^{-1}$ and $\mathbf{O}$ denote the IFFT and zero matrices, respectively. The indices at the bottom right of each matrix notation are the size of that square matrix meaning number of rows and columns. The last T_{GI} rows insert zero samples as a ZP (GI) at the end of sub-slot.

Eventually, the transmitted signal for the μth user (utilizing R subcarriers in total) is derived as

$$\mathbf{X}_\mu^\iota = \mathcal{F} \underbrace{\sum_{N=1}^{N_{RB}} \mathbf{B}_N \, \tilde{\mathbf{d}}_{\mu,N}^\iota}_{\mathbf{P} \, \tilde{\mathbf{d}}_\mu^\iota} = \mathcal{F} \, \mathbf{P} \, \tilde{\mathbf{d}}_\mu^\iota. \qquad (6)$$

In (6), matrix $\mathbf{P} = [\mathbf{B}_1, \mathbf{B}_2, \cdots, \mathbf{B}_{N_{RB}}]$ is defined for simplifying the notations. The duration of $\mathbf{X}_\mu^\iota$ equals $T_\iota = \mathfrak{L} + T_{GI} = MT_\rho + T_{GI}$.

3) CHANNEL MODEL

The transmitted signal given in (6) passes through a time and frequency dispersive channel and reaches to the receiver. The received signal corresponding to the $\mathbf{X}_\mu$ is determined like in [13]

$$\mathbf{Y}_\mu[n] = \sum_{v=0}^{L} h_v[n]\, \mathbf{X}_\mu[n-\tau_v]\, (e^{-j2\pi f_{d_v}n})(e^{-j2\pi f_\delta n}) + \mathbf{w}[n], \tag{7}$$

where L, h_v, τ_v, f_{d_v}, f_δ, and $\mathbf{w}$ denote the number of paths, complex quantity of the time based channel impulse of vth path, delay of vth path, Doppler shift of the vth path, CFO of the system, and zero mean additive white Gaussian noise (AWGN) with the variance of σ_n^2, respectively. If we translate (7) into a matrix form for the ιth received sub-slot, we have

$$\mathbf{Y}_\mu^\iota = \overbrace{\mathbf{H}^\iota\,\mathbf{D}^\iota\,\mathbf{C}^\iota}^{\mathcal{H}^\iota}\,\mathbf{X}_\mu^\iota + \mathbf{W}^\iota, \tag{8}$$

where $\mathcal{H}^\iota$ represents the $T_\iota \times T_\iota$ matrix of time and frequency dispersive channel for the ιth sub-slot. $\mathcal{H}^\iota$ is a contribution of $\mathbf{H}^\iota$, $\mathbf{D}^\iota$, and $\mathbf{C}^\iota$ representing the multipath channel, Doppler shift and CFO matrices, respectively.

$\mathbf{H}^\iota$ in (8) represents the $T_\iota \times T_\iota$ lower triangular Toeplitz matrix of multipath channel modeled as a FIR filter with a channel impulse response of $\mathbf{h} = [h_0, h_1, \cdots, h_L]^T$ in the time domain. It is worth noting that during one sub-slot of signal transmission and without the Doppler effect, the multipath channel impulse response is assumed to be fixed. It means that the power delay profile (PDP) of the multipath channel for $\mathbf{X}_\mu^\iota$ is fixed. This assumption is mandatory for circularity assumption of the multipath channel within duration of ιth sub-slot (T_ι) in the absence of the Doppler effect. In other words, the frequency dispersive channel is caused only by the Doppler effect. Therefore, we have

$$\mathbf{H}^\iota = \left[\begin{array}{cccc|ccc} \overbrace{h_0 \quad 0 \quad \cdots \quad 0}^{\mathbf{H}_d} & & & & \overbrace{0 \quad \cdots \quad 0}^{\mathbf{H}_{zp}} & & \\ h_0 & 0 & \cdots & 0 & 0 & \cdots & 0 \\ h_1 & \ddots & \ddots & \vdots & 0 & \cdots & \vdots \\ \vdots & \ddots & \ddots & 0 & \vdots & \ddots & 0 \\ h_L & \cdots & h_1 & h_0 & 0 & \cdots & 0 \\ 0 & \ddots & \ddots & h_1 & h_0 & \cdots & 0 \\ \vdots & \ddots & \ddots & \vdots & \vdots & \ddots & \vdots \\ 0 & \cdots & 0 & h_L & h_{L-1} & \cdots & h_0 \end{array}\right]_{T_\iota \times T_\iota}. \tag{9}$$

Regarding to the first $\mathfrak{L}$ columns of $\mathbf{H}^\iota$, the submatrix $\mathbf{H}_d$ is a Toeplitz matrix ($\mathfrak{L}$ full-rank matrix) and is always guaranteed to be invertible, which assures symbol recovery regardless of

the channel zero locations [25]–[27]. It is worth noting that $\mathbf{H}_d$ is multiplied by the non-zero part of the $\mathbf{X}_\mu^\iota$ while $\mathbf{H}_{zp}$ is multiplied by the zero portion of $\mathbf{X}_\mu^\iota$ and the result equals zero. Therefore, the circularity assumption of the multipath channel is obtained as

$$\mathbf{H}_c^\iota = \left[\begin{array}{cccc|ccc} \overbrace{h_0 \quad 0 \quad \cdots \quad 0}^{\mathbf{H}_d} & & & & \overbrace{h_{L-1} \quad \cdots \quad h_1}^{\mathbf{H}_{zp}} & & \\ h_0 & 0 & \cdots & 0 & h_{L-1} & \cdots & h_1 \\ h_1 & \ddots & \ddots & \vdots & 0 & \ddots & \vdots \\ \vdots & \ddots & \ddots & 0 & \vdots & \ddots & h_{L-1} \\ h_L & \cdots & h_1 & h_0 & 0 & \cdots & 0 \\ 0 & \ddots & \ddots & h_1 & h_0 & \cdots & 0 \\ \vdots & \ddots & \ddots & \vdots & \vdots & \ddots & \vdots \\ 0 & \cdots & 0 & h_L & h_{L-1} & \cdots & h_0 \end{array}\right], \tag{10}$$

where $\mathbf{H}_c^\iota$ is a circularized matrix form of $\mathbf{h}$ vector when $\tau_{\max} \leqslant T_{GI}$. $\mathbf{D}^\iota$, in (8), denotes the $T_\iota \times T_\iota$ lower triangular matrix which creates the Doppler effect in the channel. The Doppler effect in the frequency dispersive channel is modeled as Doppler shift denoted by f_{d_v} for v^{th} path. Similar to [28]

$$f_{d_v} = \frac{V_\mu}{V_s} f_k \cos\theta_v, \tag{11}$$

where V_μ, V_s, f_k, and θ_v represent the relative velocity, RF velocity, bandpass frequency of kth subcarrier and path angle, respectively. It is worth noting that the Doppler effect is a combination of Doppler shift and Doppler spread. However, in high speed UAV communications, increasing the V_μ causes to have larger Doppler shift than Doppler spread. Figure 6 illustrates the effect of Doppler shift over OFDM subcarriers [28]. Additionally, we assume an unknown V_μ which varies in a real environment. Thus, there are different Doppler shifts at each time instance due to the variation of V_μ. In other words, for v^{th} path, Doppler shift can be different at each time instances. Therefore, the total number of Doppler shifts which exist in one sub-slot is set as $\mathcal{Z}$. Then based on (8) and (9), we have

$$\mathbf{H}^\iota\mathbf{D}^\iota = \left[\begin{array}{cccc|cc} h_0\Gamma^{f_{d_0}} & 0 & \cdots & \vdots & \cdots & 0 \\ h_1\Gamma^{f_{d_1}} & h_0\Gamma^{f_{d_{L+1}}} & \ddots & \vdots & \ddots & \vdots \\ \vdots & \ddots & \ddots & \vdots & \ddots & \vdots \\ h_L\Gamma^{f_{d_L}} & \ddots & \ddots & \vdots & \ddots & 0 \\ 0 & h_L\Gamma^{f_{d_{2L+1}}} & \ddots & \vdots & \ddots & \vdots \\ \vdots & 0 & \ddots & \vdots & \ddots & \vdots \\ \vdots & \ddots & \ddots & \vdots & \ddots & \vdots \\ 0 & \cdots & \cdots & \vdots & \cdots & h_0\Gamma^{f_{d_{\mathcal{Z}-1}}} \end{array}\right], \tag{12}$$

where $\Gamma = e^{-j2\pi}$. Based on (8), (9), and (12), matrix $\mathbf{D}^\iota$ can be written as $\mathbf{D}^\iota = \mathbf{H}^{\iota\dagger}\mathcal{H}^\iota\mathbf{C}^{\iota-1}$ where $(.)^\dagger$ represents pseudoinverse operation. Matrix $\mathbf{C}^\iota$ in (8) is defined as the
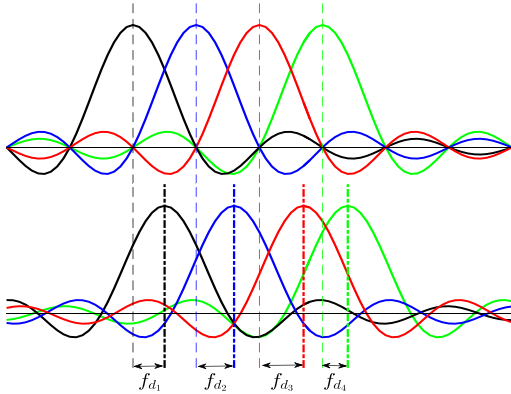
diagonal CFO matrix affecting all subcarriers equally. The entries on the diagonal of matrix $\mathbf{C}^\iota$ are assumed as the average frequency offset of the transceiver and are defined based on $\Delta f_s = \frac{1}{T_\ell}$ as follows:

$$f_\delta = \frac{\delta}{T_\ell} = \delta \, \Delta f_s, \quad \delta \in [-1, 1], \tag{13}$$

where f_δ is a fraction of reference subcarrier-spacing of Δf_s. Finally, the channel can be modeled as

$$
\begin{aligned}
&\mathcal{H}^\iota \\
&= \mathbf{H}^\iota \mathbf{D}^\iota \mathbf{C}^\iota \\
&= \begin{bmatrix}
h_0 \Gamma^{f_{d_0}+f_\delta} & 0 & \cdots & \vdots\ \cdots & 0 \\
h_1 \Gamma^{f_{d_1}+f_\delta} & h_0 \Gamma^{f_{d_{L+1}}+f_\delta} & \ddots & \vdots\ \ddots & \vdots \\
\vdots & \ddots & \ddots & \vdots\ \ddots & \vdots \\
h_L \Gamma^{f_{d_L}+f_\delta} & \ddots & \ddots & \vdots\ \ddots & 0 \\
0 & h_L \Gamma^{f_{d_{2L+1}}+f_\delta} & \ddots & \vdots\ \ddots & \vdots \\
\vdots & 0 & \ddots & \vdots\ \ddots & \vdots \\
\vdots & \ddots & \ddots & \vdots\ \ddots & \vdots \\
0 & \cdots & \cdots & \vdots\ \cdots & h_0 \Gamma^{f_{d_{\mathcal{Z}-1}}+f_\delta}
\end{bmatrix}.
\end{aligned}
\tag{14}
$$

Substituting (10) into the (14) results in $\mathcal{H}^\iota = \mathbf{H}_c^\iota \mathbf{D}^\iota \mathbf{C}^\iota$ and the received signal at (8) can be re-expressed as

$$\mathbf{Y}_\mu^\iota = \mathbf{H}_c^\iota \, \mathbf{D}^\iota \, \mathbf{C}^\iota \, \mathbf{X}_\mu^\iota + \mathbf{W}^\iota. \tag{15}$$

4) DATA RECOVERY IN LICIS
Figure 7 shows the data block diagram of the LICIS using zero forcing (ZF) equalizer. $\mathbf{Y}_\mu^\iota$, defined in (15), is the received vector which goes through a FFT block. The FFT-size of this FFT block equals the length of ιth sub-slot (T_ι). Note that the multipath channel state information is assumed to be available at the receiver side. Then, similar to the case of ZP-FAST, studied in [25], for M OFDM symbols in one

sub-slot, we have

$$\mathbf{F}_{T_\iota} \mathbf{Y}_\mu^\iota = \overbrace{\mathbf{F}_{T_\iota} \mathbf{H}_c^\iota \mathbf{F}_{T_\iota}^{-1}}^{\mathfrak{D}_h^\iota} \mathbf{F}_{T_\iota} \, \mathbf{D}^\iota \, \mathbf{C}^\iota \, \mathcal{F} \, \mathbf{P} \, \tilde{\mathbf{d}}_\mu^\iota + \overbrace{\mathbf{F}_{T_\iota} \mathbf{W}^\iota}^{\tilde{\mathcal{W}}^\iota}, \tag{16}$$

where $\mathfrak{D}_h^\iota$ is the $T_\iota \times T_\iota$ diagonal matrix of frequency response of the multipath channel. In the frequency domain, the major effect of multipath channel is removed by a FDE (ZF equalization is done in the frequency domain), and then an IFFT transforms the signal into the time domain again

$$\overbrace{\mathbf{F}_{T_\iota}^{-1} \mathfrak{D}_h^{\iota\,\dagger}}^{\mathcal{V}^\iota} \overbrace{\mathbf{F}_{T_\iota} \mathbf{Y}_\mu^\iota}^{\mathfrak{g}_\mu^\iota} = \mathbf{D}^\iota \, \mathbf{C}^\iota \, \mathcal{F} \, \mathbf{P} \, \tilde{\mathbf{d}}_\mu^\iota + \mathbf{F}_{T_\iota}^{-1} \mathfrak{D}_h^{\iota\,\dagger} \tilde{\mathcal{W}}^\iota. \tag{17}$$

This is the process of the pre-FFT multipath equalizer in LICIS. It is worth noting that this pre-FFT multipath equalizer is applied on M OFDM symbols. Also, by assuming that Doppler shifts and CFO are unknown, the result of $\mathbf{D}^\iota \mathbf{C}^\iota$ is set as an identity matrix[1] ($\mathbf{I}_{T_\iota}$). So, we have

$$\mathcal{V}^\iota \, \mathfrak{g}_\mu^\iota = \mathbf{I}_{T_\iota} \mathcal{F} \, \mathbf{P} \, \tilde{\mathbf{d}}_\mu^\iota + \mathcal{V}^\iota \, \tilde{\mathcal{W}}^\iota. \tag{18}$$

Finally, the recovered data is achieved as

$$
\begin{aligned}
\hat{\tilde{\mathbf{d}}}_\mu^\iota &= \mathbf{P}^T \, \mathcal{F}^\dagger \, \mathcal{V}^\iota \, \mathfrak{g}_\mu^\iota \\
&= \tilde{\mathbf{d}}_\mu^\iota + \mathbf{P}^T \, \mathcal{F}^\dagger \, \mathcal{V}^\iota \, \tilde{\mathcal{W}}^\iota,
\end{aligned}
\tag{19}
$$

where $\hat{\tilde{\mathbf{d}}}_\mu^\iota$ is the estimated data symbol stream in ι^{th} sub-slot for the μth user. Note that the result of $\mathcal{F}^\dagger \mathcal{V}^\iota$ is a $\mathfrak{L}$ full-rank matrix. It guarantees the ZF symbol recovery, regardless of the channel nulls (like in [25]).

In order to avoid noise enhancement in ZF equalizer, a LMSE estimation can be deployed as

$$
\begin{aligned}
&\hat{\tilde{\mathbf{d}}}_\mu^\iota \\
&= \mathbf{P}^T \, \mathcal{F}^H \, \mathbf{F}_{T_\iota}^H \, \mathfrak{D}^{\iota\,H} \left[\frac{\sigma_n^2}{\sigma_d^2} \mathbf{I}_{T_\iota} + \mathfrak{D}_h \mathbf{F}_{T_\iota} \mathcal{F} \mathcal{F}^H \mathbf{F}_{T_\iota}^H \mathfrak{D}_h^{\iota\,H} \right]^{-1} \mathfrak{g}_\mu^\iota,
\end{aligned}
\tag{20}
$$

where $(.)^H$ represents conjugate transpose operation. The estimated data symbol stream in conventional LTE numerology with ZF and LMSE equalizers are given in Appendix (31) and (32), respectively. It is evident that the LMSE estimation is more complex than ZF equalization.

C. COMPLEXITY ANALYSIS
Relaxing the constraint of unique subcarrier-spacing for the 5G numerology design has not been standardized yet. However, an extensive discussion, in [19], [20], and [29], has been done to prove that it is a low complex candidate among the presented solutions for reducing ICI. The main disadvantage of using large subcarrier-spacing is its spectral inefficiency. Furthermore, using the large subcarrier-spacing only for high speed users and small subcarrier-spacing for low

---

[1] Although estimation of $\mathbf{D}^\iota$ and $\mathbf{C}^\iota$ can improve the system performance, the complexity of the equalizer will be increased as well.
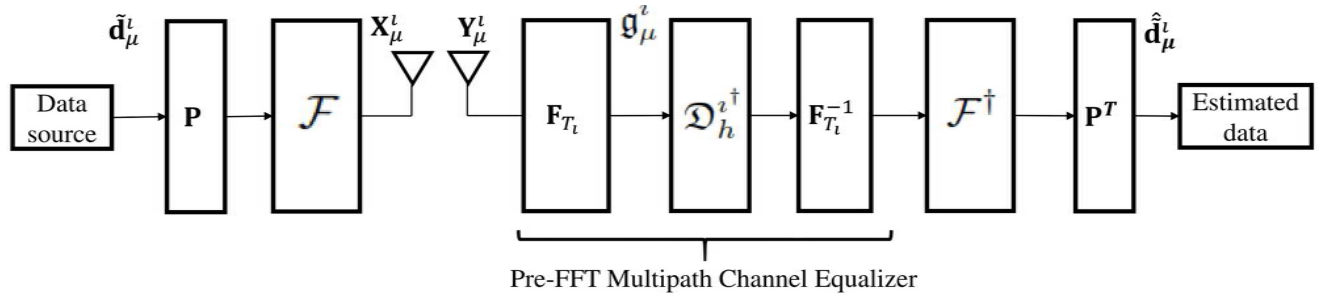
FIGURE 7. Transmitter and receiver block diagram of the LICIS.

speed users leads to different symbol durations. It changes the synchronous transmission to an asynchronous transmission. It is evident that handling the asynchronous communications has its own complex solutions (e.g., filtering each user-RB like in [15]). Regarding to these issues, LICIS provides an opportunity to use the large subcarrier-spacing transmission in a sub-slot duration for both high and low speed users without losing spectral efficiency. In other words, the proposed approach facilitates the synchronous transmission for high and low speed users. The only complexity increment of the LICIS, compared to the conventional LTE numerology, is an additional FFT and IFFT operations for the equalizer. They are the $\mathbf{F}_{T_\iota}$ and $\mathbf{F}_{T_\iota}^{-1}$ matrices given in (17). It is worth noting that the block of $\mathcal{F}$ is as complex as one IFFT block with the size of $\mathfrak{L}$ in the conventional LTE numerology. Therefore, it does not increase the complexity of the system. Table I shows the fair complexity comparison in terms of FFT and IFFT blocks in the transceivers of conventional LTE numerology and LICIS. Moreover, in case of channel estimation, the same multipath channel estimation as conventional LTE numerology is required because the Doppler shift is not estimated in LICIS and multipath channel in absence of Doppler effect is assumed to be fixed during a sub-slot duration.

TABLE 1. Complexity comparison of transceivers in conventional LTE numerology and LICIS ($M = \rho \Rightarrow T_\ell = \mathfrak{L} = \rho\, T_\rho$).

	Conventional LTE numerology	LICIS
Transmitter	one IFFT block with size of $\mathfrak{L}$	ρ IFFT blocks with size of $\frac{\mathfrak{L}}{\rho}$ ($\mathcal{F}$)
Receiver	one FFT block with size of $\mathfrak{L}$	ρ FFT blocks with size of $\frac{\mathfrak{L}}{\rho}$ one FFT block with size of T_ι one IFFT block with size of T_ι

III. SPECTRAL EFFICIENCY ANALYSIS

In the case of spectral efficiency evaluation, the number of data bits, transmitted in the time domain, is considered as a metric called data bit density (like in [30]). The data bit density of three different scenarios are compared analytically as follows:

1 Conventional numerology with reference subcarrier-spacing (Δf_s) (e.g., Figure 1)
2 Conventional numerology with large subcarrier-spacing (Δf_q) (e.g., Figure 2)
3 LICIS with subcarrier-spacing of Δf_ρ (e.g., Figure 3)

The same GI duration is considered in all three scenarios. It is a fraction of T_ℓ where $T_{GI} = \frac{T_\ell}{\kappa}$, $\kappa \in \{\mathbb{N} > 1\}$. The given BW is fixed for all the scenarios as well.

In scenario 1, the data symbols of one RB are transmitted in sub-slot duration of $T_\ell + T_{GI}$. Thus, data bit density, denoted by η_1, is as follows

$$\eta_1 = \frac{K \times \log_2 \Lambda}{(\frac{K}{2}\omega_s)(T_\ell + \frac{T_\ell}{\kappa})}, \qquad (21)$$

where Λ denotes the modulation order of the symbols. In scenario 2, the data symbols of one RB are transmitted in sub-slot duration of $\frac{T_\ell}{q} + T_{GI}$. Therefore, we have

$$\eta_2 = \frac{\frac{K}{q} \times \log_2 \Lambda}{(\frac{K}{2q}\omega_q)(\frac{T_\ell}{q} + \frac{T_\ell}{\kappa})}. \qquad (22)$$

Finally for the LICIS, the data symbols of one RB are transmitted in sub-slot duration of $M\,T_\rho + T_{GI}$ which leads to have

$$\eta_3 = \frac{M\,\frac{K}{\rho} \times \log_2 \Lambda}{(\frac{K}{2\rho}\omega_\rho)(M\,\frac{T_\ell}{\rho} + \frac{T_\ell}{\kappa})}. \qquad (23)$$

Increasing Δf_q in scenario 2 causes to decrease the symbol transmission duration. Thus, scenario 2 requires more GI than scenario 1 in a certain time period. Therefore, it is obvious that $\eta_1 > \eta_2$. The data symbol density of LICIS depends on M. Moreover, M depends on the period of time while the multipath channel is fixed, in absence of the Doppler effect, because the circularity assumption of the multipath channel in (10) is required to be satisfied during one sub-slot duration. Thus, we have

$$\begin{cases} M \geqslant \rho \Rightarrow \eta_3 \geqslant \eta_1 \\ M \geqslant \frac{\rho}{q} \Rightarrow \eta_3 \geqslant \eta_2. \end{cases} \qquad (24)$$

In conventional numerologies, the multipath channel is fixed for a one sub-slot duration ($T_\ell + T_{GI}$) in absence of the Doppler effect. It supports the circularity assumption of the multipath channel. Therefore, in the same environmental

condition for LICIS and same multipath channel estimation complexity, we can guarantee the circularity assumption of the multipath channel in period of $T_\ell + T_{GI}$. It happens where $M = \rho \Rightarrow T_\ell = \rho \frac{T_\rho}{\rho}$. Therefore, based on (24), the spectral efficiency is preserved where $M = \rho$.

IV. ICI DISTORTION EXPRESSION

In this part, the ICI distortion powers, in conventional LTE numerology and LICIS, are compared analytically. One RB of the conventional LTE numerology with subcarrier-spacing of Δf_s in a frequency dispersive channel is considered. The ICI power, which affects the ζth subcarrier in the RB, is given in [31] as

$$\mathcal{P}_{\text{ICI}_{\text{LTE}}}(\zeta) = \frac{(T_\ell f_{d_{\max}} \sigma_d)^2}{2} \sum_{r=1, r \neq \zeta}^{K} \frac{1}{(r - \zeta)^2}. \quad (25)$$

For the ICI power in LICIS model, (6) is rewritten as follows

$$
\mathbf{X}_\mu^l[n]
$$
$$
= \begin{cases} \frac{1}{\sqrt{T_\rho}} \sum_{r=\lfloor \frac{n}{T_\rho} \rfloor T_\rho}^{\left(\lfloor \frac{n}{T_\rho} \rfloor + 1\right) T_\rho} a_r e^{j \frac{2\pi}{T_\rho} \left(r - \lfloor \frac{n}{T_\rho} \rfloor T_\rho\right) n} & 0 \leqslant n \leqslant \mathfrak{L} - 1 \\ 0 & \mathfrak{L} \leqslant n \leqslant T_l - 1, \end{cases}
$$
$$(26)$$

where a_r denotes the rth data symbol in the frequency domain and $\lfloor . \rfloor$ is a floor function. Then similar to (25) for conventional LTE numerology, the following ICI power affecting the ζth subcarrier in one RB is obtained for $\mathbf{X}_\mu^l$ in LICIS:

$$\mathcal{P}_{\text{ICI}_{\text{LICIS}}}(\zeta) = \frac{(T_\rho f_{d_{\max}} \sigma_d)^2}{2} \sum_{r=1, r \neq \zeta}^{\frac{K}{\rho}} \frac{1}{(r - \zeta)^2}. \quad (27)$$

The ICI power in (27) is affected by less number of subcarriers ($\frac{K}{\rho}$) along with the smaller multiplier (T_ρ) compared to the ICI power in (25) for LTE numerology with K subcarriers and multiplier T_ℓ. Therefore, the less ICI power affects the subcarriers in LICIS and consequently better reliability is expected to be obtained.

V. NUMERICAL RESULTS

In the simulations, we compare our proposed numerology design with the conventional LTE numerology. Comparisons include: *a*) symbol error rate (SER) performance in high speed UAV communications, *b*) spectral efficiency performance, *c*) average error vector magnitude (EVM) distribution over the subcarriers, and finally *d*) ICI power versus normalized Doppler shift.

In all of the simulations with sample duration of $t_s = 0.52 \,\mu s$, the following parameters are considered: $\Delta f_s = 15 \, \text{kHz}, M = \rho, \mathfrak{L} = 128, K = 12, N_{RB} = 6, T_{GI} = 16 t_s \,\mu s$, and $\tau_{max} = 16 t_s \,\mu s$. The multipath Rayleigh fading channel is simulated as exponentially decaying power delay profile
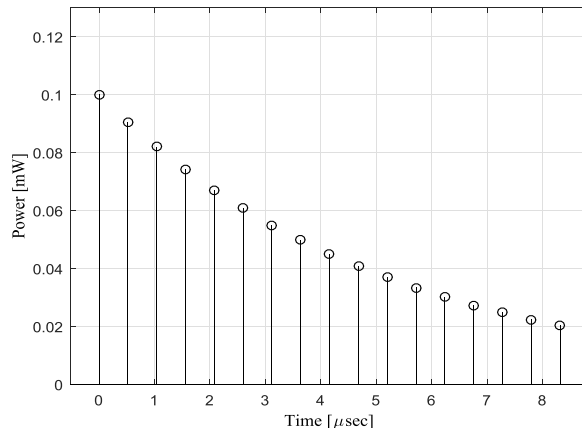

FIGURE 8. PDP of the multipath Rayleigh fading channel without Doppler effect ($\tau_{\text{max}} = 16 t_s$).

(PDP) like in Figure 8 with $\tau_{rms} = 10 t_s \,\mu s$. The CFO of the system is set as $f_\delta = 200$ Hz. The radio frequency transmission band is considered at 1 GHz.

A. SYMBOL ERROR RATE PERFORMANCE

In order to show the SER performance of the LICIS in a high speed UAV communications scenario, two different user speeds are considered as 200 km/h and 500 km/h. The maximum Doppler shift equals 1050 Hz and 2850 Hz, respectively. The Doppler shift for each subcarrier is a fraction of reference subcarrier-spacing ($\Delta f_s = 15 \,\text{kHz}$). The ratio of frequency shift over subcarrier-spacing is defined as the normalized Doppler shift.
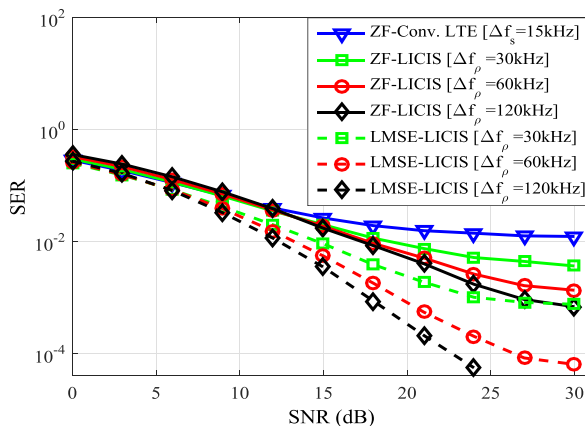

FIGURE 9. 4-QAM SER performance comparison where $V_\mu = 200$ km/h and $f_{d_{\max}} = 0.07 \Delta f_s$ ($M = \rho$).

Figure 9 depicts the SER performance of LICIS for different subcarrier-spacings compared to the conventional LTE numerology where the user speed is 200 km/h. By going toward the higher speed communications, the better understanding of SER performance improvement of the LICIS can be concluded as shown in Figure 10. LICIS with the subcarrier-spacing of $\Delta f_\rho = 120$ kHz gains a remarkable performance improvement compared to the conventional LTE

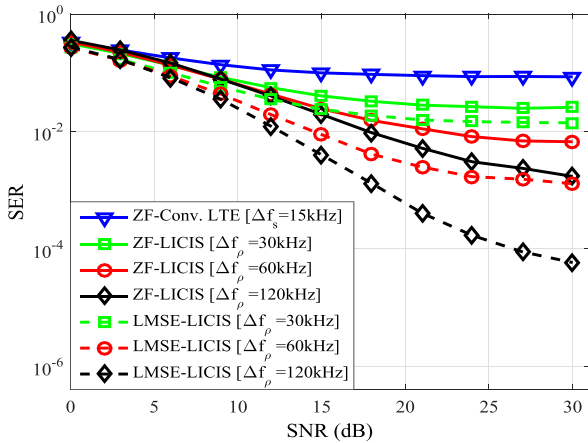**FIGURE 10.** 4-QAM SER performance comparison where $V_\mu = 500$ km/h and $f_{d_{max}} = 0.19\Delta f_s$ ($M = \rho$).
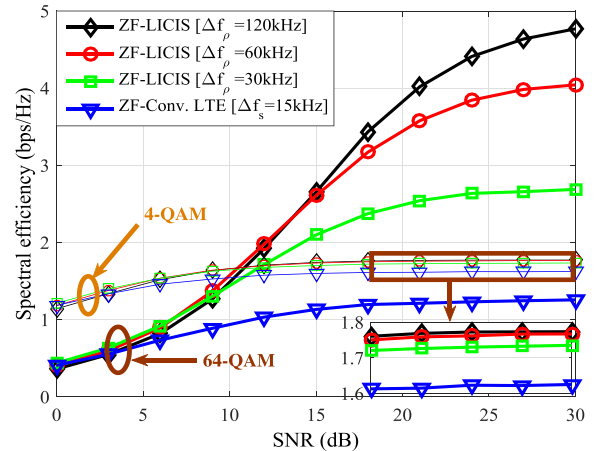

FIGURE 12. 64-QAM and 4-QAM spectral efficiency performance comparison where $V_\mu = 500$ km/h and $f_{d_{max}} = 0.19\Delta f_s$ ($M = \rho$).
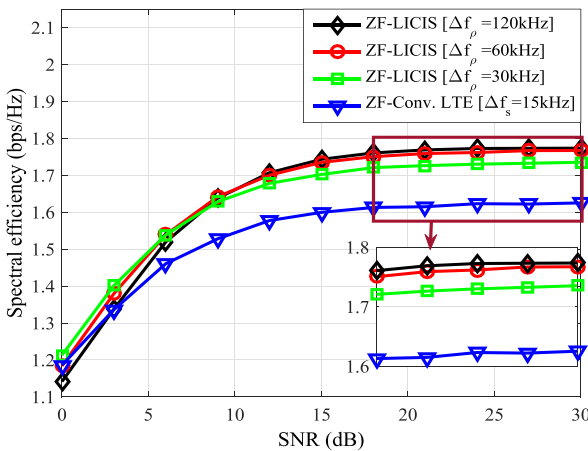

FIGURE 11. 4-QAM spectral efficiency performance comparison where $V_\mu = 500$ km/h and $f_{d_{max}} = 0.19\Delta f_s$ ($M = \rho$).
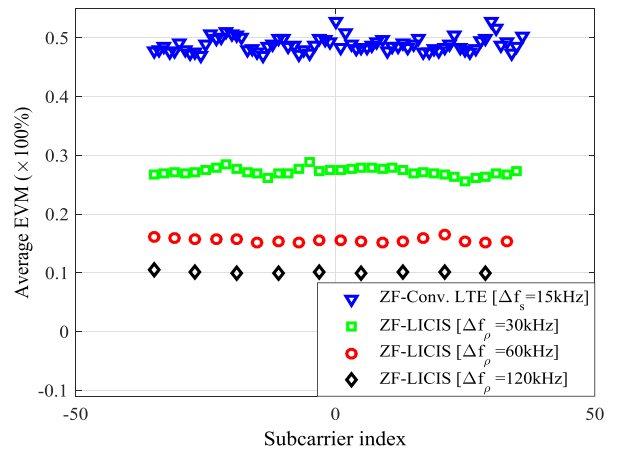

FIGURE 13. 4-QAM EVM distribution comparison where $V_\mu = 500$ km/h and $f_{d_{max}} = 0.19\Delta f_s$.

numerology with ZF equalizer. Indeed, this is obtained by utilizing 8 times larger subcarrier-spacing than the reference subcarrier-spacing.

B. SPECTRAL EFFICIENCY EVALUATION

Figure 11 compares the spectral efficiency of the LICIS and conventional LTE numerology in the high speed UAV communications where the user speed is $V_\mu = 500$ km/h. The 4-QAM modulation is used in this simulation and consequently $\Lambda = 4$. The LICIS, with $\Delta f_\rho = 120$ kHz, outperforms the conventional LTE numerology around 10% in high SNRs. The superior improvement of the spectral efficiency in LICIS compared to the conventional LTE numerology is observed in Figure 12 where the higher QAM modulation order such as 64-QAM is used ($\Lambda = 64$). It is worth noting that the conventional LTE numerology with 64-QAM even has worse spectral efficiency performance than 4-QAM in UAV communications with speed of $V_\mu = 500$ km/h. It happens due to the high sensitivity of conventional LTE symbol boundary alignment numerology to the severe Doppler shifts.

C. AVERAGE ERROR VECTOR MAGNITUDE DISTRIBUTION

In order to see how the subcarriers are located and how ICI problem affects the EVM, the average EVM for each subcarrier is given in Figure 13 where $V_\mu = 500$ km/h. As shown in this figure, in the conventional LTE numerology, subcarriers have small subcarrier-spacing ($\Delta f_s = 15$ kHz) but there are more subcarriers in a given BW. By going toward the LICIS and increasing subcarrier-spacing (Δf_ρ) the number of subcarriers decreases in the BW. As a result, the EVM due to the ICI on each subcarrier decreases remarkably. Furthermore, the less subcarriers leads to have less peak to average power ratio which is an advantage in power amplifier selection as well.

D. ICI POWER VERSUS NORMALIZED DOPPLER SHIFT

Figure 14 confirms the accuracy of the LICIS analysis where the analytical ICI power for one subcarrier closely agrees with the simulation results. It illustrates the variation of ICI power for one subcarrier versus the normalized Doppler shift. It is evident that by increasing the normalized Doppler shift,
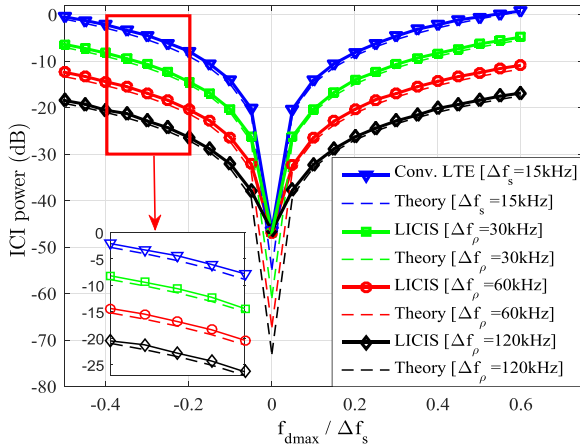
FIGURE 14. Simulation and theoretical results for the ICI power on a subcarrier versus normalized frequency Doppler shift.

the ICI power increases. However, the increment of the ICI power in LICIS with $\Delta f_\rho = 120$ kHz is outstandingly (around 18 dB) less than the conventional LTE numerology.

VI. CONCLUSIONS

In this work, a novel symbol boundary alignment with respect to OFDM waveform is proposed to reduce the ICI while preserving the spectral efficiency. The analytical forms of the ICI power and spectral efficiency are derived and closely match with the simulation results in the time-frequency dispersive channel. e.g., around 18 dB ICI power reduction along with the 10% spectral efficiency enhancement compared to the conventional LTE numerology is achieved with subcarrier-spacing of 120 kHz and 4-QAM modulation in high speed UAV communications. Furthermore, the complexity increment of LICIS is compared to the conventional LTE system and results in an acceptable complexity increment compared to that of already existing solutions. Additionally, it is in compatibility with the current radio access numerologies. Other potential advantage of LICIS is that it utilizes less subcarriers in a given BW compared to the conventional LTE numerology leading to a lower peak to average power ratio and consequently requires less complex power amplifiers as well. In general, the LICIS is a spectral efficient solution with a reasonable complexity increment for the ICI problem in high speed UAV communications. Moreover, LICIS can be utilized in other high speed applications as well, such as high speed train communications.

APPENDIX

DATA RECOVERY IN CONVENTIONAL LTE NUMEROLOGY

In Conventional LTE numerology the ιth stream of modulated data symbols related to the μth user ($\tilde{\mathbf{d}}_\mu^\iota$) are inserted in the desired subcarriers by matrix $\mathbf{P}$ and then go through an IFFT with IFFT-size of $\mathfrak{L}$. The OFDM symbol is modeled as

$$\mathbf{X}_{\mu_{\text{lte}}}^\iota = \mathbf{F}_\mathfrak{L}^{-1}\mathbf{P}\tilde{\mathbf{d}}_\mu^\iota. \qquad (28)$$

Then CP is appended to avoid ISI. This CP also leads to circularity assumption of the multipath channel as it is

explained in [25]. After passing through the channel like in (8) and at the receiver side, the CP is removed from the received signal. The remained signal is

$$\mathbf{Y}_{\mu_{\text{LTE}}} = \mathbf{H}_{c_\mathfrak{L}}^\iota\,\mathbf{D}_\mathfrak{L}^\iota\,\mathbf{C}_\mathfrak{L}^\iota\,\mathbf{F}_\mathfrak{L}^{-1}\mathbf{P}\tilde{\mathbf{d}}_\mu^\iota + \mathbf{W}_\mathfrak{L}^\iota. \qquad (29)$$

Note that the multipath, Doppler and CFO matrices in (15) are $T_\iota \times T_\iota$ square matrices. However, they are changed to $\mathfrak{L} \times \mathfrak{L}$ square matrices in (29) because CP is removed and consequently the length of the signal is decreased. The length of the noise vector $\mathbf{W}^\iota$ in (8) is decreased to the $\mathfrak{L}$ for $\mathbf{W}_\mathfrak{L}^\iota$ in (29) as well. $\mathbf{Y}_{\mu_{\text{lte}}}$ goes through a FFT. Then, with the same assumption of $\mathbf{D}_\mathfrak{L}^\iota\,\mathbf{C}_\mathfrak{L}^\iota = \mathbf{I}_\mathfrak{L}$ like in (18), we have

$$\mathbf{F}_\mathfrak{L}\mathbf{Y}_{\mu_{\text{LTE}}} = \mathbf{F}_\mathfrak{L}\mathbf{H}_{c_\mathfrak{L}}^\iota\mathbf{I}_\mathfrak{L}\mathbf{F}_\mathfrak{L}^{-1}\mathbf{P}\tilde{\mathbf{d}}_\mu^\iota + \mathbf{F}_\mathfrak{L}\mathbf{W}_\mathfrak{L}^\iota$$
$$= \mathfrak{D}_{h_\mathfrak{L}}^\iota\mathbf{P}\tilde{\mathbf{d}}_\mu^\iota + \mathbf{F}_\mathfrak{L}\mathbf{W}_\mathfrak{L}^\iota. \qquad (30)$$

Then, the estimated data with ZF equalizer is

$$\hat{\tilde{\mathbf{d}}}_\mu^\iota = \mathbf{P}^T\mathfrak{D}_{h_\mathfrak{L}}^{\iota\dagger}\mathbf{F}_\mathfrak{L}\mathbf{Y}_{\mu_{\text{LTE}}}$$
$$= \tilde{\mathbf{d}}_\mu^\iota + \mathbf{P}^T\mathfrak{D}_{h_\mathfrak{L}}^{\iota\dagger}\mathbf{F}_\mathfrak{L}\mathbf{W}_\mathfrak{L}^\iota. \qquad (31)$$

To avoid the noise enhancement in ZF equalizer, the LMSE equalizer can be deployed. Then, we have

$$\hat{\tilde{\mathbf{d}}}_\mu^\iota = \mathbf{P}^T\mathfrak{D}_{h_\mathfrak{L}}^{\iota H}\left[\frac{\sigma_n^2}{\sigma_d^2}\mathbf{I}_\mathfrak{L} + \mathfrak{D}_{h_\mathfrak{L}}^\iota\mathfrak{D}_{h_\mathfrak{L}}^{\iota H}\right]^{-1}\mathbf{F}_\mathfrak{L}\mathbf{Y}_{\mu_{\text{LTE}}}. \qquad (32)$$

REFERENCES

[1] H. Lin, "Flexible configured OFDM for 5G air interface," *IEEE Access*, vol. 3, pp. 1861–1870, 2015.

[2] N. Tadayon, G. Kaddoum, and R. Noumeir, "Inflight broadband connectivity using cellular networks," *IEEE Access*, vol. 4, pp. 1595–1606, 2016.

[3] K. Sankar. *Inter Carrier Interference (ICI) in OFDM Due to Frequency Offset.* Accessed: Aug. 2009. [Online]. Available: http://www.dsplog.com/2009/08/08/effect-of-ici-in-ofdm/

[4] J. Wu and P. Fan, "A survey on high mobility wireless communications: Challenges, opportunities and solutions," *IEEE Access*, vol. 4, pp. 450–476, 2016.

[5] C. R. Sheu, J. W. Liu, and C. C. Huang, "A low complexity ICI cancellation scheme with multi-step windowing and modified SIC for high-mobility OFDM systems," in *Proc. IEEE 71st Veh. Technol. Conf.*, Taipei, Taiwan, May 2010, pp. 1–5.

[6] J. Armstrong, "Analysis of new and existing methods of reducing intercarrier interference due to carrier frequency offset in OFDM," *IEEE Trans. Commun.*, vol. 47, no. 3, pp. 365–369, Mar. 1999.

[7] K. Y. Lin, H. P. Lin, and M. C. Tseng, "An equivalent channel time variation mitigation schefme for ICI reduction in high-mobility OFDM systems," *IEEE Trans. Broadcast.*, vol. 58, no. 3, pp. 472–479, Sep. 2012.

[8] X. Li, R. Zhou, V. Chakravarthy, S. Hong, and Z. Wu, "Total intercarrier interference cancellation for OFDM mobile communication systems," in *Proc. 7th IEEE Consum. Commun. Netw. Conf.*, Las Vegas, NV, USA, Jan. 2010, pp. 1–5.

[9] N. Aboutorab, W. Hardjawana, and B. Vucetic, "A new iterative Doppler-assisted channel estimation joint with parallel ICI cancellation for high-mobility MIMO-OFDM systems," *IEEE Trans. Veh. Technol.*, vol. 61, no. 4, pp. 1577–1589, May 2012.

[10] S.-M. Tseng, "An iterative ICI cancellation and decoding scheme for coded OFDM systems in mobile channels," *IEICE Trans. Fundam. Electron., Commun. Comput. Sci.*, vol. E88-A, no. 11, pp. 3085–3091, Nov. 2005.

[11] S. U. Hwang, J. H. Lee, and J. Seo, "Low complexity iterative ICI cancellation and equalization for OFDM systems over doubly selective channels," *IEEE Trans. Broadcast.*, vol. 55, no. 1, pp. 132–139, Mar. 2009.

[12] M. Nakamura, M. Itamit, K. Itoh, and H. Aghvami, "ICI cancellation technique based on estimating delay and Doppler profile in OFDM reception," *J. Inst. Image Inf. Television Eng.*, vol. 56, no. 12, pp. 1951–1958, 2002.

[13] Z. Mokhtari and M. Sabbaghian, "Near-optimal angle of transform in FrFT-OFDM systems based on ICI analysis," *IEEE Trans. Veh. Technol.*, vol. 65, no. 7, pp. 5777–5783, Jul. 2016.

[14] K. Kambara, H. Nishimoto, T. Nishimura, T. Ohgane, and Y. Ogawa, "Subblock processing in MMSE-FDE under fast fading environments," *IEEE J. Sel. Areas Commun.*, vol. 26, no. 2, pp. 359–365, Feb. 2008.

[15] V. Vakilian, T. Wild, F. Schaich, S. ten Brink, and J.-F. Frigon, "Universal-filtered multi-carrier technique for wireless systems beyond LTE," in *Proc. IEEE Globecom Workshops (GC Wkshps)*, Atlanta, GA, USA, Dec. 2013, pp. 223–228.

[16] A. R. Jafri, J. Majid, M. A. Shami, M. A. Imran, and M. Najam-Ul-Islam, "Hardware complexity reduction in universal filtered multicarrier transmitter implementation," *IEEE Access*, vol. 5, pp. 13401–13408, 2017.

[17] T. Wild, F. Schaich, and Y. Chen, "5G air interface design based on universal filtered (UF-)OFDM," in *Proc. 19th Int. Conf. Digit. Signal Process.*, Hong Kong, 2014, pp. 699–704.

[18] *Numerology Requirements*, document R1-162204, Qualcomm Incorporated, Busan, South Korea, Apr. 2016. [Online]. Available: http://www.3gpp.org/ftp/TSG_RAN/WG1_RL1/TSGR1_84b/Docs/R1-162204.zip

[19] *Numerology Evaluation Results for High Speed Scenario*, document R1-166939, ETRI, Gothenburg, Sweden, Aug. 2016. [Online]. Available: http://www.3gpp.org/ftp/tsg_ran/WG1_RL1/TSGR1_86/Docs/R1-166939.zip

[20] G. Berardinelli, K. I. Pedersen, F. Frederiksen, and P. E. Mogensen, "On the design of a radio numerology for 5G wide area" in *Proc. 11th Int. Conf. Wireless Mobile Commun. (ICWMC)*, 2015, pp. 13–18.

[21] Keysight Technol., Inc. (2017). *LTE Physical Layer Overview*. [Online]. Available: http://rfmw.em.keysight.com/wireless/helpfiles/89600b/webhelp/subsystems/lte/content/lte_overview.htm

[22] *NR Numerologies*, document R1-167027, KT Corp, Gothenburg, Sweden, Aug. 2016. [Online]. Available: http://www.3gpp.org/ftp/tsg_ran/WG1_RL1/TSGR1_86/Docs/R1-167027.zip

[23] W. Rhee, N. Xu, B. Zhou, and Z. Whang, "Fractional-N frequency synthesis: Overview and practical aspects with FIR-embedded design," *J. Semicond. Technol. Sci.*, vol. 13, no. 2, pp. 170–183, Apr. 2013.

[24] Y. S. Cho, J. Kim, W. Y. Yang, and C. Kang, "Introduction to OFDM," in *Mimo-OFDM Wireless Communications With MATLAB*, 1st ed. Hoboken, NJ, USA: Wiley, 2010, ch. 4, sec. 2, pp. 128–135.

[25] B. Muquet, Z. Wang, G. B. Giannakis, M. D. Courville, and P. Duhamel, "Cyclic prefixing or zero padding for wireless multicarrier transmissions?" *IEEE Trans. Commun.*, vol. 50, no. 12, pp. 2136–2148, Dec. 2002.

[26] A. Scaglione, G. B. Giannakis, and S. Barbarossa, "Redundant filterbank precoders and equalizers. II. Blind channel estimation, synchronization, and direct equalization," *IEEE Trans. Signal Process.*, vol. 47, no. 7, pp. 2007–2022, Jul. 1999.

[27] J. H. Manton and Y. Hua, "A frequency domain deterministic approach to channel identification," *IEEE Signal Process. Lett.*, vol. 6, no. 12, pp. 323–326, Dec. 1999.

[28] S. Ahmed and H. Arslan, "Evaluation of frequency offset and Doppler effect in terrestrial RF and in underwater acoustic OFDM systems," in *Proc. IEEE Military Commun. Conf. (MILCOM)*, San Diego, CA, USA, Nov. 2008, pp. 1–7.

[29] G. Wunder *et al.*, "5GNOW: Non-orthogonal, asynchronous waveforms for future mobile applications," *IEEE Commun. Mag.*, vol. 52, no. 2, pp. 97–105, Feb. 2014.

[30] B. Farhang-Boroujeny, "OFDM versus filter bank multicarrier," *IEEE Signal Process. Mag.*, vol. 28, no. 3, pp. 92–112, May 2011.

[31] T. Wang, J. G. Proakis, E. Masry, and J. R. Zeidler, "Performance degradation of OFDM systems due to Doppler spreading," *IEEE Trans. Wireless Commun.*, vol. 5, no. 6, pp. 1422–1432, Jun. 2006.

MAHYAR NEMATI (S'17–M'17) was born in Arak, Iran, in 1992. He received the B.S. degree in electrical engineering in telecommunications from the University of Tehran, Tehran, Iran, in 2015. He is currently pursuing the M.S. degree in electrical, electronics, and cyber systems with Istanbul Medipol University. He is currently a Research Assistant with the Communication, Signal Processing and Networking Center, Istanbul Medipol University, where he involved in the field of wireless communication. His research interests include digital communications, signal processing techniques at the physical and medium access layer, multi-carrier schemes, waveform design in wireless networks, and software defined radio systems.

HÜSEYIN ARSLAN (S'95–M'98–SM'04–F'15) received the B.S. degree from Middle East Technical University, Ankara, Turkey, in 1992, and the M.S. and Ph.D. degrees from Southern Methodist University, Dallas, TX, USA, in 1994 and 1998, respectively. From 1998 to 2002, he was with the Research Group of Ericsson Inc., NC, USA, where he was involved in several projects related to 2G and 3G wireless communication systems. Since 2002, he has been with the Electrical Engineering Department, University of South Florida, Tampa, FL, USA. Since 2014, he has been the Dean of the College of Engineering and Natural Sciences, Istanbul Medipol University. He was a part-time consultant for various companies and institutions including Anritsu Company, Morgan Hill, CA, USA and Scientific and Technological Research Council of Turkey. His current research interests are on physical layer securities, mm-wave communications, small cells, multicarrier wireless technologies, co-existence issues on heterogeneous networks, aeronautical (high-altitude platform) communications and in vivo channel modeling, and system designs.

• • •